Flexure of the lithosphere beneath the north polar cap of Mars, with implication for ice compositions and heat flow

Adrien Pierre Michel Broquet[1], Mark A. Wieczorek[1], and Wenzhe Fa[2]

[1]Observatoire de la Côte d'Azur
[2]Peking University

November 23, 2022

Abstract

The geodynamical response of the lithosphere under stresses imposed by the geologically young north polar cap is one of the few clues we have to constrain both its composition and the present-day thermal state of Mars. Here we combine data from orbital radar sounders with a lithospheric loading model to self-consistently estimate the density (ρ) and real dielectric constant (ε) of the polar cap, and the elastic thickness of the lithosphere underneath (Te). We show that ρ can range from 920 to 1520 kg m, ε is constrained to be 2.75 (+0.40,-0.35), and Te is found to range from 330 to 450 km. We determine an updated polar cap volume that is up to 30% larger than current estimates that all neglect lithospheric flexure. Inferred compositions suggest that a minimum of 10% CO is buried in the deposits, which may have important implications for the climate evolution of Mars.

Flexure of the lithosphere beneath the north polar cap of Mars, with implication for ice compositions and heat flow

A. Broquet[1]*, M. A. Wieczorek[1], W. Fa[2,3]

[1]Université Côte d'Azur, Observatoire de la Côte d'Azur, CNRS, Laboratoire Lagrange, Nice, France.
[2]Institute of Remote Sensing and Geographical Information System, School of Earth and Space Sciences, Peking University, Beijing, China.
[3]State Key Laboratory of Lunar and Planetary Sciences, Macau University of Science and Technology, Macau, China.

Key Points:

- Radar data and a loading model are used to probe the composition of the north polar cap of Mars and the strength of the lithosphere.
- The elastic thickness beneath the polar cap is found to range from 330 to 450 km, implying heat flows of 11 to 16 mW m^{-2}.
- At least 10% CO_2 ice must be present within the polar cap to be consistent with our estimated density and real dielectric constant.

Corresponding author: A. Broquet, `adrien.broquet@oca.eu`

Abstract

The geodynamical response of the lithosphere under stresses imposed by the geologically young north polar cap is one of the few clues we have to constrain both its composition and the present-day thermal state of Mars. Here we combine data from orbital radar sounders with a lithospheric loading model to self-consistently estimate the density (ρ) and real dielectric constant (ε) of the polar cap, and the elastic thickness of the lithosphere underneath (T_e). We show that ρ can range from 920 to 1520 kg m^{-3}, ε is constrained to be 2.75 (+0.40, -0.35), and T_e is found to range from 330 to 450 km. We determine an updated polar cap volume that is up to 30% larger than current estimates that all neglect lithospheric flexure. Inferred compositions suggest that a minimum of 10% CO_2 is buried in the deposits, which may have important implications for the climate evolution of Mars.

Plain Language Summary

The north polar cap of Mars is a tremendous reservoir of ices and dust of unknown concentration and composition. It is transparent to radar giving us a unique insight into its structure and composition. Here we use a novel technique that combines radar and elevation data along with a flexure model, to probe the basement of the north polar cap and jointly invert for its composition and the strength of the underlying lithosphere. Similar to previous studies, we find that the lithosphere below the north pole is extremely rigid and doesn't deform much under the load of the polar cap. This implies that the north polar region is currently colder than the rest of the planet, which has profound implications for our understanding of the structure and evolution of the Martian interior. Inferred compositions suggest that a minimum of 10% CO_2 is buried in the deposits. This is the first time a large quantity of CO_2 ice is constrained to exist in the north polar cap. Like on Earth, where the composition of buried ices gives hints on the climatic evolution, having CO_2 at the north pole of Mars will help improve scenarios for the climate evolution of the planet.

1 Introduction

The Martian north polar cap has long been recognized to be a tremendous reservoir of water ice and possibly dry ice or even clathrate-hydrates (Mellon, 1996). The geologically young (< 1 Ma, see Herkenhoff & Plaut, 2000; Levrard et al., 2007) polar cap plays a significant role in the present-day Martian climate, and its stratigraphically layered deposits are a witness to the planet's climate evolution (Phillips et al., 2001). The cap further acts as a large scale load that can bend the underlying and surrounding basement. Analysis of the associated lithospheric flexure is one of the few methods that give access to the composition of the polar cap and to the present-day strength of the lithosphere, which is related to the thermal state of the planet (e.g. Phillips et al., 2008; Plesa et al., 2018).

Sounding radar data from MARSIS (Mars Advanced Radar for Subsurface and Ionosphere Sounding) on Mars Express and SHARAD (SHAllow RADar) onboard Mars Reconnaissance Orbiter have been used to unveil the structure of the north polar deposits and to map the ice/substratum interface. The two instruments operate at frequencies of 1.3−5.5 MHz and 20 MHz, allowing to probe depths from several hundreds of meters to kilometers with range resolutions in vacuum of 150 m for MARSIS (Picardi et al., 2005) and 15 m for SHARAD (Phillips et al., 2008). The bulk of the north polar cap is made of the north polar layered deposits that are thought to consist of nearly pure water ice (Grima et al., 2009; Selvans et al., 2010). These deposits overlay a basal unit with a more limited extent and whose composition is believed to have a relatively larger quantity of dust (Herkenhoff et al., 2007; Nerozzi & Holt, 2019). Both MARSIS and SHARAD observed a general lack of downward deflection below the north polar cap with uncertainties of about 200 m everywhere (Selvans et al., 2010), and 100 m across Gemina Lingula (Phillips et al., 2008) (Figure 1).

The absence of measurable lithospheric flexure in these previous studies suggests that the thickness of the elastic lithosphere is more than 300 km and that Mars might be colder than once thought (Phillips et al., 2008). The joint spectral analysis of gravity and topography also constrained the present-day elastic thickness for the south pole to be high, at least 108 km (Wieczorek, 2008). These high (and potentially different) elastic thickness values at the north and south poles are difficult to reconcile with current thermal evolution models (e.g. Plesa et al., 2018), unless the bulk concentration of heat-producing elements (HPE) in the Martian interior is less than chondritic (Phillips et al., 2008).

These inferences, however, could be potentially flawed given that there are significant uncertainties that could hide the signal of lithospheric deflection. The global uncertainty on the basal deflection given by analyses of MARSIS data from Selvans et al. (2010) was for a single value of the real dielectric constant (ε), where it was assumed that the whole polar cap was made of nearly pure water ice with $\varepsilon = 3$. As the polar cap thickness scales as $1/\sqrt{\varepsilon}$, varying ε can significantly increase this uncertainty. The study of Phillips et al. (2008) used the global topography as a load when predicting the deflection of the lithosphere and the presence of a long-wavelength signal arising from the broad Tharsis volcanic province could potentially bias the lithospheric deflection beneath the polar cap. Lastly, we note that constraints on the composition of the polar cap were obtained by assuming that its base is flat and inverting for the real dielectric constant using MOLA elevation and radar data (e.g. Grima et al., 2009; Nerozzi & Holt, 2019). If the base were deflected downward, this would require a lower bulk dielectric constant of the polar cap and modify the inferred compositions.

In this study, we combine MARSIS, SHARAD, and MOLA elevation data with an improved elastic loading model to jointly invert for the elastic thickness of the lithosphere underneath the north polar cap along with the density and real dielectric constant of the polar cap. We refine and give a more robust elastic thickness estimate that will help to constrain interior models using data from the InSight mission (Plesa et al., 2018; Smrekar et al., 2018). We further give a new estimate of the north polar cap volume, which is higher than previous studies that neglected lithospheric flexure. We finally constrain that there must be some CO_2 ice buried deep within the north polar perennial cap, which may have important implications for the climate evolution of Mars.

2 Inversion for elastic thickness, density and real dielectric constant

We invert for the elastic thickness of the lithosphere (T_e), the polar cap load density (ρ), and the real part of the dielectric constant by minimizing the root-mean-square (rms) misfit of the function

$$\psi(\varepsilon, T_e, \rho) = [\mathrm{h_e} - \mathrm{h_0} - \mathrm{W}(T_e, \rho)] - \mathrm{h_t}(\varepsilon). \tag{1}$$

In this equation, $\mathrm{h_e}$ is surface elevation, $\mathrm{h_0}$ is an estimated pre-loading surface topography, W is the computed deflection of the polar cap basement, and $\mathrm{h_t}$ is the thickness of the polar cap derived from radar data. All terms depend implicitly on position. The first term in square brackets represents the thickness of the polar cap at a given location based on the surface elevation and lithospheric deflection and is dependent on the density of the polar cap and the elastic thickness. The last term is a measurement of the thickness from radar data, which depends on the assumed dielectric constant.

For our calculations, it is necessary to have an estimate of the shape of the surface before the polar cap formed. The pre-loading surface ($\mathrm{h_0}$) was estimated using an annulus of MOLA elevation data (Smith et al., 2001) exterior to the polar cap between 70°N to 75°N (see also Selvans et al., 2010) and these data were interpolated poleward using the minimum curvature method of Smith and Wessel (1990). The pre-loading surface follows the long-wavelength regional topography that slopes from high values north of Arabia Terra near 90°E towards Alba Mons near 270°E (Figure S1). We note that varying the annulus latitudinal limits by ±2° introduces an uncertainty of only 170 m in the shape of the basement.

The radar thickness ($\mathrm{h_t}$) was derived from MARSIS and SHARAD data. We picked manually 213 locations that are spatially scattered across the polar deposits, investigated all available radargrams, and identified visually the reflections arising from the icy surface and the ice/substratum interface. The surface reflectors were selected as those echoes with the strongest amplitude and with the shortest time delay and the deepest subsurface reflectors were identified as the strongest echoes with the largest time delay (Figure S2). For each location, the lateral continuity of the surface and subsurface reflectors were verified to extend at least 7 frames along the orbital track. The thickness is calculated using the time delay from the surface and subsurface echoes (t) and then converting the result into a distance by assuming a value for the real dielectric constant

$$\mathrm{h_t} = \frac{\mathrm{tc}}{2\sqrt{\varepsilon}}. \tag{2}$$

where c is the speed of light in vacuum.

The elastic deflection (W) is computed iteratively. We first define the load as the thickness derived from MOLA and the initial pre-loading surface ($\mathrm{h_e} - \mathrm{h_0}$), and then iterate by adding the amount of corresponding deflected materials. Typically, only a few iterations are necessary to converge to sub-meter accuracies. As in Phillips et al. (2008), the densities of the crust and mantle were set to 2900 and 3500 kg m^{-3} respectively, the crustal thickness was set to 35 km, Young's modulus was set to 100 GPa, and Poisson's ratio was assumed to be 0.25. We note that reasonable variations of these parameters do not influence the computed deflection significantly.

3 Thickness and deflection below the polar deposits

In Figure 1 (left), we plot an estimate of the thickness of the north polar cap using MOLA surface elevation data with no lithospheric deflection. The thickness of the polar cap under these assumptions has a maximum value of 3120 m and a total volume of 1.31×10^6 km^3, which are consistent with earlier studies (e.g. Selvans et al., 2010). Superposed on this image we plot the polar cap thickness as determined by 213 MARSIS measurements, with the fill color corresponding to the same color scale as the main image, and where we have assumed that $\varepsilon = 3$ (e.g., Selvans et al., 2010). Given that the spacecraft orbit is not perfectly polar, there are no observations poleward 87°N. A good overall agreement between the estimated thickness and radar measurements is seen. Small differences are likely due to local variations in dielectric constant and/or to lithospheric deflection beneath the polar deposits. We also investigated SHARAD data and observed that the thickness predictions are in good agreement with MARSIS when the basal unit is not present. SHARAD cannot generally see through the entirety of the basal unit as a result of its sand-rich deposits (see Text S1 and Figure S2 and Nunes & Phillips, 2006).

On the right panel of Figure 1, we reproduce the deflection of the lithosphere from Phillips et al. (2008) in red, for an elastic thickness of 300 km and a surface density of 1100 kg m^{-3}. The deflection using our model for the same parameters is shown in white and is due solely to the isolated load of the polar cap. Though both contours fit the condition of less than 100 m of relative deflection across Gemina Lingula, there are significant differences. The deflection of Phillips et al. (2008) is offset from the center of the polar cap, with about 400 m of deflection near the center and more than 350 m of deflection outside of the polar cap. In comparison, the deflection computed from our model is centered on the polar cap has a slightly smaller central value of 320 m, and has less than 150 m of deflection outside of the polar cap.

We found that this difference was due to Phillips et al. (2008) using the global topography as a load (with a constant density of 1100 kg $^{-3}$) in the deflection model, causing the presence of an unwanted long-wavelength signal originating from the broad Tharsis province. It is clear that Tharsis formed billions of years before the polar cap was emplaced and that its induced flexure is unrelated to the flexure resulting from the geologically young polar cap. Even if there is an ancient flexural signature resulting from Thar-

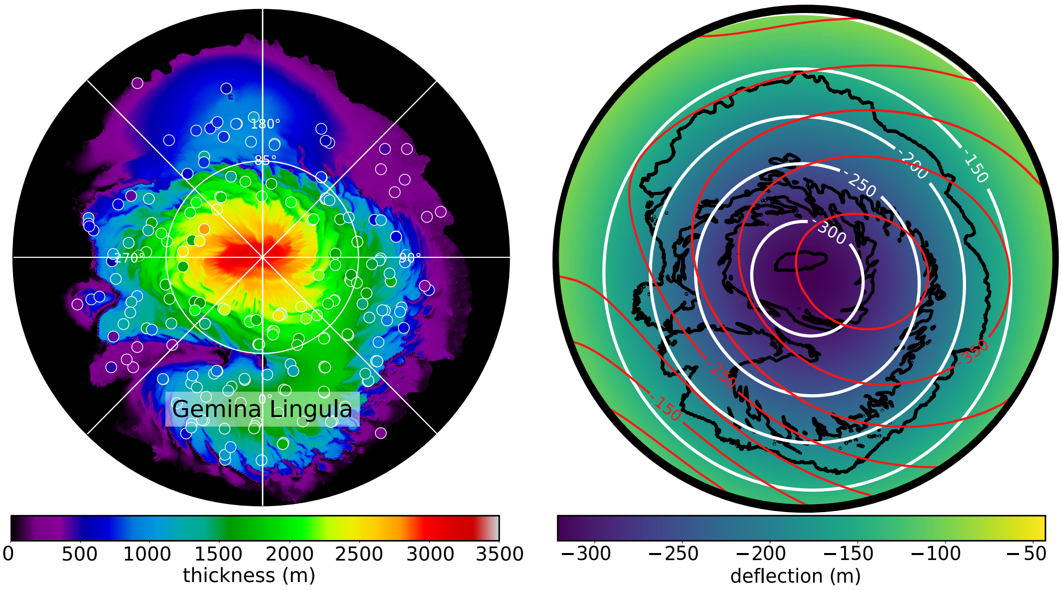

Figure 1. (left) Estimated thickness of the north polar cap from MOLA surface elevations under the assumption that the base of the cap follows the regional slope. The filled colored circles correspond to the thickness obtained at 213 regions from MARSIS radargrams. (right) Computed lithospheric deflection from our model (color map and white contour) and that of Phillips et al. (2008) (red contours), for $T_e = 300$ km and $\rho = 1100$ kg m^{-3}. For context, elevation contours of the polar cap are plotted as black lines.

sis in the north polar region, this signal would not bias our results, given that our polar cap load is defined with respect to the regional topographic slope.

4 Results

We show in Figure 2 the minimum misfit of eq. 1 in color as a function of two parameters and for any value of the third parameter. The misfit was computed using MARSIS data at 213 locations, of which the number is more than sufficient to obtain robust estimates and uncertainties of the three free parameters in our inversion (see Figure S3). The rms misfit is cutoff at 266 m, which is the maximum allowed misfit in the estimation of the thickness of the polar cap that includes the range resolution of MARSIS, surface roughness at the scale of the Fresnel zone of MARSIS and the uncertainty in the estimation of the pre-loading surface (see Text S2 for more details).

We observe that the dielectric constant is allowed to range from 2.00 (the minimum value investigated) to 3.25 with a best-fit of about 2.75, the elastic thickness must be greater than 180 km, and the density must be less than 1700 kg m^{-3}. The minimum required elastic thickness is significantly lower than the 300 km obtained by Phillips et al. (2008) as a result of the improved loading model, though we will see that including additional constraints on the inversion that were not considered by Phillips et al. (2008) will require an increase in the minimum elastic thickness. We note that when assuming zero deflection (i.e., an infinite elastic thickness), the obtained dielectric constant is 3.14$\pm$ 0.35, which is similar to that found in Grima et al. (2009) who assumed zero deflection.

Parts of the colored regions of Figure 2 correspond to densities and real dielectric constants that cannot be simultaneously obtained by mixtures of ices and dust. A Maxwell-Garnett mixing law (Sihvola, 2000) was used to compute the bulk dielectric constant where we assumed that the matrix was the component with the largest volumetric abundance. We note that the results would be similar using a power-law mixing relation as in Nerozzi and Holt (2019). The dielectric constants for solid CO_2, H_2O ice, and dust were set to 2.2, 3 and 6 respectively, and the densities of solid CO_2 and water ice were assumed to be 1560 and 920 kg m^{-3}. The density of the dust component was allowed to vary from 2200 to 3400 kg m^{-3}, which covers the range from gypsum to basalt (Nunes & Phillips, 2006). The range of solutions that fit the data and that can also be accounted for by a mixture of these three components are outlined by the black dashed line in this figure. The range of permissible values for the dielectric constant is reduced to 2.2 to 3.15, the minimum elastic thickness is increased to 330 km, and the maximum density is reduced to 1600 kg m^{-3}.

We further note that the thermal conductivity of the polar cap is strongly dependent on the relative abundances of ices and dust (Mellon, 1996; Wieczorek, 2008). If the effective thermal conductivity is low enough, this could result in temperatures that would be sufficient to melt the base of the cap (see Text S3 for more details). In regions covered by radar observations, there is no evidence for a melt layer being present today. We thus assume that basal melting is not presently occurring. The orange and red dashed lines delimit the allowable compositions that do not generate basal melting under typical heat flows of 20 and 25 mW m^{-2} (Plesa et al., 2018). For a heat flow of 20 mW m^{-2}, the dielectric constant is found to range from 2.40 to 3.15, the elastic thickness is found to be independent of heat flow with a value of at least 330 km, and the density is found to range from 920 to 1520 kg m^{-3}. The obtained range of densities is in good agreement with gravity studies at the north (Ojha, Nerozzi, & Lewis, 2019) and south pole (Wieczorek, 2008; Zuber et al., 2007) where the bulk density of both caps was found to be about 1200 $\pm$ 150 kg m^{-3}.

We performed an independent inversion using SHARAD data, but only at 78 restricted locations where the basal unit is not present and where the base of the polar cap is clearly visible (Figure S2). The results we obtained were generally consistent with those presented above, but with a slightly higher elastic thickness and lower dielectric constant (Figure S4). As an example, for a heat flow of 20 mW m^{-2}, the dielectric constant was allowed to range from 2.4 to 3.0, the elastic thickness was found to be at least 370 km, and the surface density was constrained to be less than 1570 kg m^{-3}.

We note that the only way to lower the elastic thickness at the north pole would be to simultaneously reduce the density and dielectric constant of the mixture. This could be achieved by adding some porosity, and for 2 or 5% porosity, the minimum elastic thickness would be reduced to respectively 300 and 280 km. On Earth, typical volume fraction of bubbles in glacial ice at an equivalent Martian depth of 1200 m is only about 0.5% (Fegyveresi et al., 2016), so the presence of porosity would likely have only a small effect on our inversion results.

In Figure 3, we show a map of the polar cap and several profiles across Chasma Boreale. Chasma Boreale is a deep trough that separates the main lobe of the north polar cap from Gemina Lingula (Figure 3). Radar studies have shown that the basal unit is exposed at the bottom of Chasma Boreale where it is only about 150 m thick (Selvans et al., 2010; Holt et al., 2010; Putzig et al., 2009). Using SHARAD data, we confirmed that the thickness of the basal unit in the two deepest troughs of Chasma Boreale is about 150 m. These two troughs are located close to the center of the polar cap, where the basement is potentially subject to a large deflection that is comparable to the thickness of the deposits. This makes these two locations remarkably sensitive to variations in elastic thickness such that we decided to treat them separately.

The bottom panel of Figure 3 plots several profiles including the surface elevation as defined by MOLA (blue), the pre-loading surface (red), and the deflection profiles for various elastic thicknesses (black). The two orange dots correspond to the base of the basal unit given by SHARAD in the two deepest troughs of Chasma Boreale that is 150

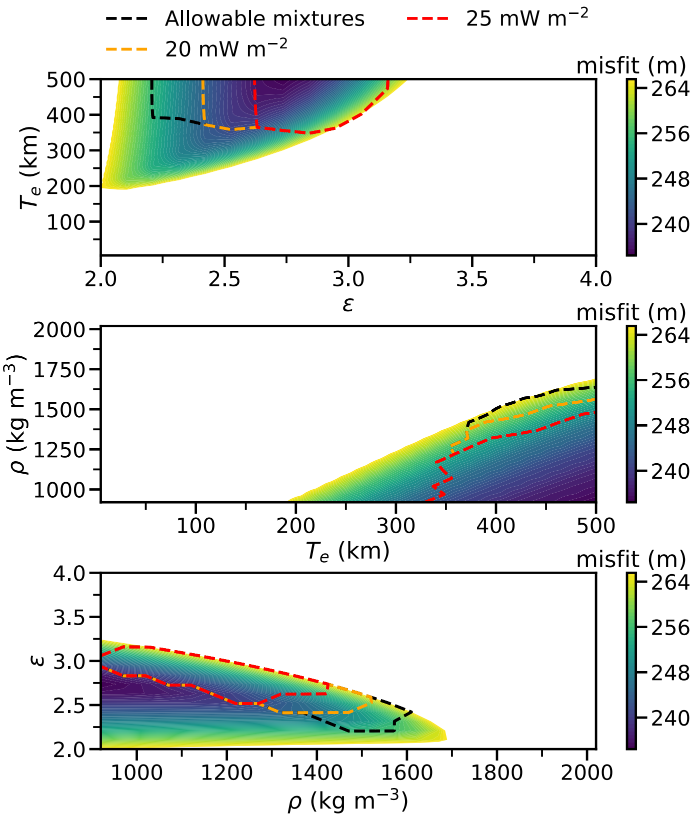

Figure 2. Minimum rms misfit as a function of the dielectric constant (ε), elastic thickness (T_e), and bulk density of the polar cap (ρ) using MARSIS data at 213 locations. The color corresponds to the rms misfit that is cut off at 266 m. The black lines delimit possible mixtures, and the red and orange lines delimit those same mixtures that do not produce basal melting for heat flows of 20 and 25 mW m^{-2}.

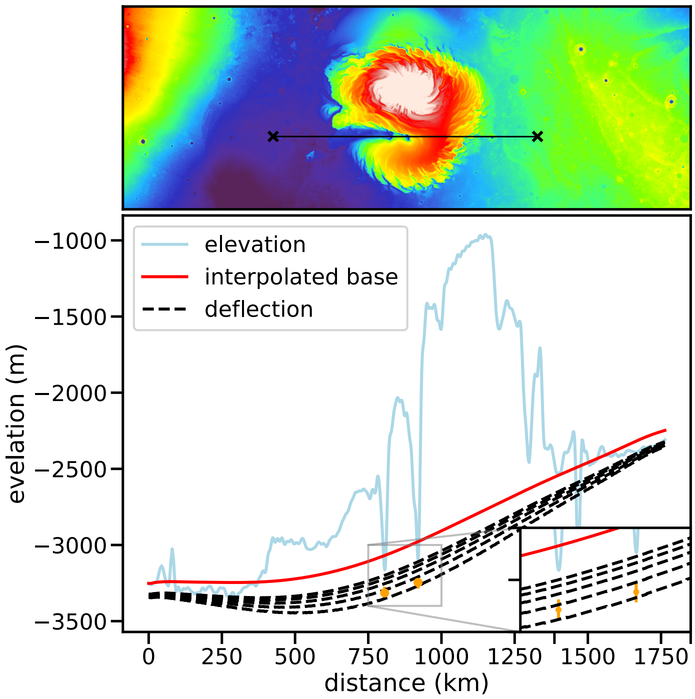

Figure 3. Surface and deflection profiles across Chasma Boreale. The profile section is shown in the upper image and in the lower image, we display an elevation profile based on MOLA data (blue), a profile for the interpolated basement (red), and plausible profiles arising from lithospheric deflection (dashed black). The deflection profiles were computed for $T_e = 300$ (lower) to 500 (upper) km with 50 km increments and $\rho = 1100$ kg m^{-3}. The inset shows details regarding two SHARAD measurements of the base of the polar cap (orange).

m below the local surface elevation given by MOLA. At both locations, we have considered a 42 m depth uncertainty that corresponds to plausible variations in the dielectric constant (from 2.5 to 3.5), the surface roughness, and the range resolution of SHARAD. At these locations, we observe that the pre-loading surface is about 230 m above the basement depth given by SHARAD. A small amount of deflection of the surface is thus required to account for these measurements. Based on the plotted deflection profiles, we observe that the elastic thickness has a best fit of about 330 km and cannot be larger than 400 km. We note that if the load density is set to the highest allowed value (1520 kg m^{-3}), then the largest allowable elastic thickness is 450 km.

5 Composition of the north polar cap

To address the composition of the north polar cap, we assumed that the polar cap is homogeneous, and explored which fractions of H_2O and CO_2 ices, and dust (clathrates are treated in Text S4 and Figure S5) could fit both our density and dielectric constant estimates. Given that both parameters are dependent on the elastic thickness, we show three results in Figure 4 for three different elastic thicknesses (330, 350 and 400 km). Each plot is a ternary diagram that shows the range of allowable compositions, where the color provides the corresponding real dielectric constant of the mixture. In all cases, we observe that the north pole is made mostly of pure water ice and that high heat flows require a low solid CO_2 content to not melt the base of the cap.

For an elastic thickness of 330 or 350 km, we observe that there must be at least 10% dry ice within the north polar deposits and that the dielectric permittivity of the allowed compositions ranges from 2.7 to 2.9. Only the larger elastic thickness of 400 km allows for a solid CO_2 free polar cap when the dust content is less than 5%. The maximum volume of dust in the polar cap is found to depend upon the elastic thickness and dust density and varies from 5 to 28%. If the polar cap does not contain CO_2, but instead clathrate ices, there must be at least 77% clathrate ices for a heat flow of 20 mW m^{-2}, which is unlikely (Figure S5).

6 Discussion

Using the formalism of McNutt (1984) and accounting for HPE in the crust and mantle (Hahn et al., 2011), the minimum 330 and maximum 450 km elastic thicknesses can be shown to imply surface heat flows of 16 and 11 mW m^{-2} (see Text S4). In a re-

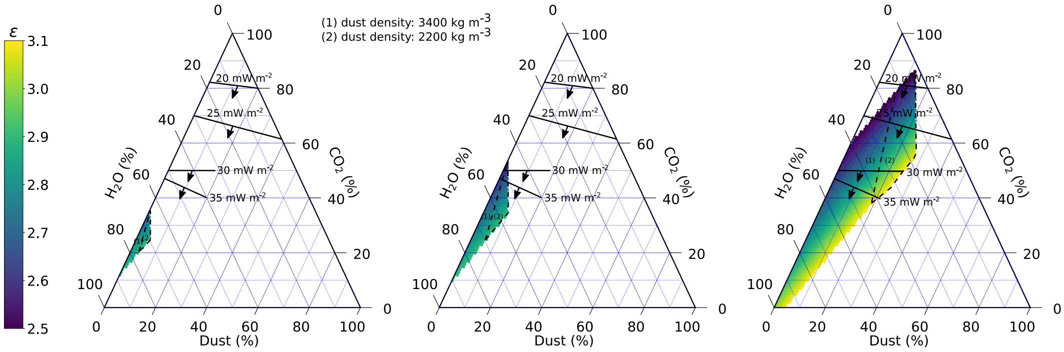

Figure 4. Ternary plot for allowable volumetric mixtures of ices and dust for three elastic thicknesses, 330, 350 and 400 km (from left to right), where the color corresponds to the real dielectric constant. The black lines limit the regions above witch basal melting will occur as a function of various heat flows from 20 to 35 mW m^{-2}, and dashed lines show the accepted mixtures that must be added if the dust density is decreased from 3400 (1) to 2200 (2) kg m^{-3}. Acceptable solutions are in the direction given by the black arrows.

cent study, Ojha, Karimi, et al. (2019) computed lithospheric deflection profiles beneath the north polar cap as a function of heat flow using a more sophisticated finite element method with a visco-elastoplastic rheology. Our results imply a maximum absolute deflection of 400 m at the center of the polar cap and 250 m below Gemina Lingula. From Figure 2 of Ojha, Karimi, et al. (2019), our constraints require the heat flow to be 13 to 20 mW m^{-2}, which is in good agreement with the heat flows computed using the approach of McNutt (1984).

Using previously reported radar constraints on the amount of lithospheric deflection beneath the north polar cap, Ojha, Karimi, et al. (2019), however, inferred a considerably lower heat flow of 7 mW m^{-2}. This discrepancy is largely the result of their having mistook previously reported relative deflections between two points with the maximum absolute deflection below the deposit. For example, the maximum deflection at the center of the cap, as predicted by both Phillips et al. (2008) and this study is about 350-400 m. Ojha, Karimi, et al. (2019) however used a value of 200 m, but this value (Selvans et al., 2010) represents only the relative deflection from the edge of the cap to about halfway to the center of the polar cap. Where the cap is thicker than 1 km, Selvans et al. (2010) noted that the maximum absolute deflection could be as high as 500 m. In a suite of thermal evolution models, Plesa et al. (2018) investigated how the thickness of the crust (which is enriched in HPE) affects the thickness of the lithosphere. For these models, an elastic thickness of more than 330 km at the north pole was compatible with an average crustal thickness of at least 62 km. If the concentration of HPE in the crust is twice the reference value given by gamma-ray spectroscopy measurements (e.g. Hahn et al., 2011), one model with a lower crustal thickness (29.5 km) satisfies our constraints on T_e. Thus, if the crust was more enriched at depth, their minimum crustal thickness estimation could easily be relaxed (Thiriet et al., 2018).

There are a few complications to our model that could perhaps provide a lower elastic thickness at the north pole. It is possible that the polar cap load is not yet at elastic equilibrium but is rather in a transient state, undergoing downward deflection, as a result of viscous relaxation. In this case, we would only be observing a fraction of the final deflection and we would overestimate the elastic thickness. The north polar region could also be experiencing some level of post-glacial rebound (upward deflection) from a former larger cap that is competing with the present-day deflection. The presently observed deflection would then be the sum of these two components, which would again lead to an overestimation of the elastic thickness. The influence of these two, possibly on-going, effects depend upon the viscosity of the mantle that is yet poorly constrained (Plesa et al., 2018) (see Text S5 and Figure S6).

In our simulations, the maximum allowed central deflection of the lithosphere is about 400 m and less than 200 m outside of the polar cap, giving a maximum cap thickness of about 3500 m. For our range of acceptable solutions, the deflected volume ranges from 0.19 to 0.41 $\times$ 10^6 km^3, and the total north polar cap volume is 1.51 to 1.73 $\times$ 10^6 km^3, which is 15% to 30% higher than previous estimates (Selvans et al., 2010).

The inferred compositions suggest that there must be at least 10% of solid CO_2 (0.15 to 0.17 $\times$ 10^6 km^3, 59 to 67 mbar) within the polar cap, the rest being water ice. Adding some dust to the polar cap would require an even larger solid CO_2 content. Because of the strong feedback between the polar caps and the atmosphere, having an important amount of sequestered CO_2, ten times larger than what was detected at the south pole (Phillips et al., 2011), has important implications on the reconstruction and prediction of the climate evolution of the planet (Levrard et al., 2007).

References

Fegyveresi, J. M., Alley, R. B., Fitzpatrick, J. J., Cuffey, K. M., McConnell, J. R., Voigt, D. E., ... Stevens, N. T. (2016). Five millennia of surface temperatures and ice core bubble characteristics from the wais divide deep core, west antarctica. *Paleoceanography*, *31*(3), 416-433. doi: https://doi.org/10.1002/2015PA002851

Grima, C., Kofman, W., Mouginot, J., Phillips, R. J., Hérique, A., Biccari, D., ... Cutigni, M. (2009). North polar deposits of Mars: Extreme purity of the water ice. *Geophysical Research Letters*, *36*(L03203). doi: https://doi.org/10.1029/2008GL036326

Hahn, B. C., McLennan, S. M., & Klein, E. C. (2011). Martian surface heat production and crustal heat flow from Mars Odyssey Gamma-Ray spectrometry. *Geophysical Research Letters*, *38*(14). doi: https://doi.org/10.1029/2011GL047435

Harper, M., et al. (2015). python-ternary: Ternary plots in python. *Zenodo*. doi: https://doi.org/10.5281/zenodo.34938

Herkenhoff, K. E., Byrne, S., Russell, P. S., Fishbaugh, K. E., & McEwen, A. S. (2007). Meter-scale morphology of the north polar region of mars. *Science*, *317*(5845), 1711–1715. doi: https://doi.org/10.1126/science.1143544

Herkenhoff, K. E., & Plaut, J. J. (2000). Surface Ages and Resurfacing Rates of the Polar Layered Deposits on Mars. *Icarus*, *144*(2), 243-253. doi: https://doi.org/10.1006/icar.1999.6287

Holt, J., E Fishbaugh, K., Byrne, S., Christian, S., Tanaka, K., S Russell, P., ... J Phillips, R. (2010, 05). The construction of chasma boreale on mars. *Nature*, *465*, 446-9. doi: https://doi.org/10.1038/nature09050

Levrard, B., Forget, F., Montmessin, F., & Laskar, J. (2007). Recent formation and evolution of northern martian polar layered deposits as inferred from a global climate model. *Journal of Geophysical Research: Planets*, *112*(E6). doi: https://doi.org/10.1016/10.1029/2006JE002772

McNutt, M. K. (1984). Lithospheric flexure and thermal anomalies. *Journal of Geophysical Research: Solid Earth*, *89*(B13), 180–194. doi: https://doi.org/10.1029/JB089iB13p11180

Mellon, M. T. (1996). Limits on the co2 content of the martian polar deposits.

Icarus, *124*(1), 268 - 279. doi: https://doi.org/10.1006/icar.1996.0203

Nerozzi, S., & Holt, J. (2019). Buried ice and sand caps at the north pole of mars: revealing a record of climate change in the cavi unit with sharad. *Geophysical Research Letters*, *0*. doi: https://doi.org/10.1029/2019GL082114

Nunes, D. C., & Phillips, R. J. (2006). Radar subsurface mapping of the polar layered deposits on mars. *Journal of Geophysical Research: Planets*, *111*(E6). doi: https://doi.org/10.1029/2005JE002609

Ojha, L., Karimi, S., Lewis, K. W., Smrekar, S. E., & Siegler, M. (2019). Depletion of heat producing elements in the martian mantle. *Geophysical Research Letters*. doi: https://doi.org/10.1029/2019GL085234

Ojha, L., Nerozzi, S., & Lewis, K. (2019). Compositional constraints on the north polar cap of mars from gravity and topography. *Geophysical Research Letters*, *0*. doi: https://doi.org/10.1029/2019GL082294

Phillips, R. J., Davis, B. J., Tanaka, K. L., Byrne, S., Mellon, M. T., Putzig, N. E., … Seu, R. (2011). Massive CO2 Ice Deposits Sequestered in the South Polar Layered Deposits of Mars. *Science*, *332*(6031), 838–841. doi: https://doi.org/10.1126/science.1203091

Phillips, R. J., Zuber, M. T., Smrekar, S. E., Mellon, M. T., Head, J. W., Tanaka, K. L., … Marinangeli, L. (2008). Mars North Polar Deposits: Stratigraphy, Age, and Geodynamical Response. *Science*, *320*(5880), 1182–1185. doi: https://doi.org/10.1126/science.1157546

Phillips, R. J., Zuber, M. T., Solomon, S. C., Golombek, M. P., Jakosky, B. M., ., W. B. B., … II, S. A. H. (2001). Ancient geodynamics and global-scale hydrology on Mars. *Science*, *291*(5513), 2587–2591. doi: https://doi.org/10.1126/science.1058701

Picardi, G., Plaut, J. J., Biccari, D., Bombaci, O., Calabrese, D., Cartacci, M., … Zampolini, E. (2005). Radar soundings of the subsurface of Mars. *Science*, *310*(5756), 1925–1928. doi: https://doi.org/10.1126/science.1122165

Plesa, A.-C., Padovan, S., Tosi, N., Breuer, D., Grott, M., Wieczorek, M. A., … Banerdt, W. B. (2018). The thermal state and interior structure of mars. *Geophysical Research Letters*, *45*(22), 12,198-12,209. doi: https://doi.org/10.1029/2018GL080728

Putzig, N. E., Phillips, R. J., Campbell, B. A., Holt, J. W., Plaut, J. J., Carter,

L. M., ... Seu, R. (2009). Subsurface structure of planum boreum from mars reconnaissance orbiter shallow radar soundings". *Icarus*, *204*(2), 443 - 457. doi: https://doi.org/10.1016/j.icarus.2009.07.034

Selvans, M. M., Plaut, J. J., Aharonson, O., & Safaeinili, A. (2010). Internal structure of Planum Boreum, from Mars advanced radar for subsurface and ionospheric sounding data. *Journal of Geophysical Research: Planets*, *115*(E9). doi: https://doi.org/10.1029/2009JE003537

Sihvola, A. (2000, Oct 01). Mixing rules with complex dielectric coefficients. *Subsurface Sensing Technologies and Applications*, *1*(4), 393–415. doi: https://doi.org/10.1023/A:1026511515005

Smith, & Wessel. (1990). Gridding with continuous curvature splines in tension. *Geophysics*, *55*(3), 293-305. doi: https://doi.org/10.1190/1.1442837

Smith, Zuber, M. T., Frey, H. V., Garvin, J. B., Head, J. W., Muhleman, D. O., ... Sun, X. (2001). Mars Orbiter Laser Altimeter: Experiment summary after the first year of global map- ping of Mars. *Journal of Geophysical Research: Planets*, *106*(E10), 23689–23722. doi: https://doi.org/10.1029/2000JE001364

Smrekar, S. E., Lognonné, P., Spohn, T., Banerdt, W. B., Breuer, D., Christensen, U., ... Wieczorek, M. (2018). Pre-mission insights on the interior of mars. *Space Science Reviews*, *215*(1), 3. doi: https://doi.org/10.1007/s11214-018-0563-9

Thiriet, M., Michaut, C., Breuer, D., & Plesa, A.-C. (2018). Hemispheric dichotomy in lithosphere thickness on Mars caused by differences in crustal structure and composition. *Journal of Geophysical Research: Planets*, *123*(4), 823-848. doi: https://doi.org/10.1002/2017JE005431

Wieczorek, M. A. (2008). Constraints on the composition of the Martian south polar cap from gravity and topography. *Icarus*, *196*, 506–517. doi: https://doi.org/10.1016/j.Icarus.2007.10.026

Zuber, M. T., Phillips, R. J., Andrews-Hanna, J. C., Asmar, S. W., Konopliv, A. S., Lemoine, F. G., ... Smrekar, S. E. (2007). Density of Mars' South Polar Layered Deposits. *Science*, *317*(5845), 1718–1719. doi: https://doi.org/10.1126/science.1146995

Acknowledgments

A.B. would like to Isaac Smith for helpful discussions. The radar data and the polar cap thickness as predicted by MOLA used in this paper are available at https://doi.org/10.5281/zenodo.3530693. The radar and topography data used in this paper are available on the PDS website (http://pds-geosciences.wustl.edu/). A.B. conceived the study with M.W., A.B. and W.F. analyzed the radar data, and all authors contributed to drafting the manuscript. W. Fa is supported by Beijing Municipal Science and Technology Commission (Z191100004319001), and the contribution of M.W. is supported by the French Space Agency (CNES). This is InSight contribution number 149. The ternary plots were made using the python-ternary package of Harper et al. (2015).

Supporting Information for “Flexure of the lithosphere beneath the north polar cap of Mars, with implication for ice compositions and heat flow”

A. Broquet[1]*, M. A. Wieczorek[1], W. Fa[2,3]

[1]Université Côte d’Azur, Observatoire de la Côte d’Azur, CNRS, Laboratoire Lagrange, Nice, France.

[2]Institute of Remote Sensing and Geographical Information System, School of Earth and Space Sciences, Peking University, Beijing, China.

[3]State Key Laboratory of Lunar and Planetary Sciences, Macau University of Science and Technology, Macau, China.

Contents of this file

1. Text S1 to S5
2. Figures S1 to S6

Introduction. In this supporting information, we compare SHARAD and MARSIS data, discuss the uncertainties in the inversion, show an additional inversion using SHARAD data, and detail some of the processing steps to constrain the composition of the north polar cap. We conclude showing a simple viscoelastic model in order to estimate whether the north polar cap is at elastic equilibrium.

Text S1: MARSIS versus SHARAD

We investigated SHARAD data to ensure that they were in good agreement with our thickness estimates using MARSIS, as SHARAD generally has a better range resolution than MARSIS. On the left of Figure S2, we show as filled circles, the differences between the apparent thickness of the north polar cap derived using MARSIS and SHARAD. Points filled in white represent locations where we did not find a subsurface echo in SHARAD radargrams. We observe a bimodal distribution, where the SHARAD thickness estimates are consistent with MARSIS in places where the basal unit is not predicted to be present below the north polar layered deposits, and largely different where the basal unit is present (for a map of the extent of the basal unit, see Selvans et al., 2010). We interpret this as a limitation of the resolution of SHARAD, which is not always able to penetrate through the sand-rich basal unit (see also Nunes & Phillips, 2006). Where there is no basal unit, the average apparent difference between MARSIS and SHARAD is 45 meters and the standard deviation is 131 meters, which is close to the 150 meters range resolution of MARSIS in free-space.

On the right side, we show examples of radar echo strengths as a function of the apparent depth at two locations, one where the basal unit is present below the north polar layered deposits (top) and one in Gemina Lingula, where the basal unit is not present (bottom). The two locations are displayed as triangles on the left image. In the upper image, we observe that the first associated with reflections from the surface (fixed at a depth of 0 km) and the top of the basal unit (depth 2.1 km) correlate well between MARSIS and SHARAD. A slight offset of about 150 meters between the peak associated with the top of the basal unit is noticed, which is likely due to the difference in range resolution of the two instruments. However, the SHARAD radargram does not show evidence for a third peak that is associated with the base of the polar cap as seen by MARSIS. In the bottom plot, we observe that the echoes from the surface and base of the polar cap of SHARAD and MARSIS correlated well, through we again do have slight offsets that are comparable to the range resolutions of the instruments. An intermediate peak between these two reflectors is also seen and is likely due to layering in the polar cap (the basal unit is not believed to be present in this region, Selvans et al., 2010). In this frame, we note that there is a deeper peak at an apparent depth of 3.3 km (corresponding to about 300 meters below the base of the polar cap) for both SHARAD and MARSIS, but this reflector showed no continuity in adjacent frames and was hence interpreted as a spurious subcrustal reflector.

Text S2: Uncertainties in the inversion

In order to place bounds on the range of acceptable parameters in our inversions, it is necessary to define a maximum allowable rms misfit between our model and the observations. Several sources of uncertainty will contribute to this value.

First, the inherent range resolution of a radar in free-space is approximately half its wavelength. For MARSIS, which has an instantaneous frequency of 1 MHz (Picardi et al., 2005), the uncertainty in free-space is 150 m and is 86.5 m in water ice ($\varepsilon = 3$).

A second source of uncertainty comes from surface roughness along an interface. The roughness of the surface can cause multiple reflections and scattering of the radio wave that makes the subsurface echo appear as a wide peak. Picking the subsurface reflector location (in unit of time) in the radargrams will then be associated with an uncertainty that is about the pulse width of the echo. The pulse width of the peaks associated with the surface and subsurface echoes for MARSIS are generally about 3 pixels or 321 m in free-space and 185 m in water ice (see Figure S2). We verified that this value, to be used as an uncertainty, is reasonable by computing the surface roughness of MOLA elevation data at the scale of the Fresnel zone. The Fresnel zone gives the typical length at which a radio wave interacts with the surrounding media and can be estimated as $2 \times \sqrt{D\lambda/2}$, where D is the distance of the spacecraft from the surface and λ its wavelength. For MARSIS, D over the north pole is about 900 km, which gives a Fresnel zone diameter of 23 km. The surface roughness of the north polar cap within 23 km diameter circles was found to vary from few meters where the polar cap is smoothest to 250 m near the edge of the polar cap and troughs, which is consistent with the estimation using the pulse width.

A third source of uncertainty comes from the shape of the pre-loading surface. To determine the uncertainty in the pre-loading surface, we varied the limits of the annulus of topographic data exterior to the polar cap used in the interpolation. We obtained that the pre-loading surfaces differed by no more than 170 m on average beneath the polar cap.

Assuming these three sources of error are independent, the rms uncertainty in the inversion for MARSIS is 266 m. For SHARAD, the uncertainties are: 8.6 m for the range resolution in water ice, 40 m uncertainty from the pulse width of the subsurface echoes (that is in good agreement with the surface roughness at the 3 km scale of the Fresnel zone), and the 170 m uncertainty from the basal interpolation. This gives an rms error of

175 m. These uncertainties are generally higher than those found in Selvans et al. (2010) (200 m for MARSIS) or Phillips et al. (2008) (100 m for SHARAD), because of the large uncertainty from the estimation of the pre-loading surface.

Text S3: Constraints on the composition of the north polar cap

CO_2 ice has a smaller thermal conductivity than water ice, which would give rise to higher internal temperatures within the polar can that could lead to basal melting. Basal melting, however, has not been observed from radar studies at the north pole. We therefore added the constraint that no basal melting should occur at present-day where radar observations are present. We used a Maxwell-Garnett mixing law to compute the thermal conductivity of mixtures (Sihvola, 2000) and solved for the temperature gradient using Fourier's law of heat conduction. In the mixing law, it was assumed that the matrix was the component with the largest volumetric abundance and that the two others were considered as randomly spaced spherical inclusions. From the temperature profiles, we checked whether the melting point of CO_2 ($\sim$ 216 K) was exceeded (H_2O has a warmer melting point, $\sim$ 273 K). Heat flows from 20 to 35 mW m^{-2} were employed (Plesa et al., 2018), a surface temperature of 155 K was assumed, and thermal conductivities of 4, 0.75, 0.75, and 3 W m^{-1} K^{-1} were used for H_2O, CO_2, clathrates and dust (Wieczorek, 2008).

A Maxwell-Garnett mixing law for a three-phase mixture was used when computing the dielectric constant of mixtures. For water ice, we used a dielectric constant of 3 (see experimental data by Pettinelli et al., 2003; Phillips et al., 2008). A real dielectric constant of 3 is the value used by the MARSIS team for water ice (Selvans et al., 2010), whereas a value of 3.15 is usually used by the SHARAD team (Grima et al., 2009). Increasing the dielectric constant of water ice would increase the amount of both CO_2 and clathrate ices in the polar cap that is predicted by our model. We also set a dielectric constant of 2.2, 2.85 and 6, respectively for CO_2 and clathrate ices, and dust (Wieczorek, 2008; Nunes & Phillips, 2006).

With two constraints (density and dielectric constant), it would be possible to invert only for the abundances of mixtures of two components uniquely. Here, we consider 3 component mixtures, and plot the possible solutions in a ternary diagram. As we consider 4 possible components (CO_2, water ice, dust, and clathrates), we show 3 separate ternary diagrams were one of the four components was assumed to be absent. The range of allowable density and dielectric constant vary as a function of the elastic thickness, and therefore, in this figure, we show two end-member cases for an elastic thickness of 330 (top) and 400 (bottom) km. We observe that in all cases, the north polar cap has a minimum of 24% to 42% water ice if we ignore models that generate basal melting for heat flows of 20 to 25 mW m^{-2}. The plots in the left column are described in the main text. If there is no CO_2 inside the north polar cap, but instead clathrate ices, then there must be a minimum of 77% to 58% of clathrates within the polar cap for heat flows of 20 to 25 mW m^{-2}.

Text S4: Conversion of elastic thickness to heat flow

The method to convert an elastic thickness into a heat flow was pioneered by McNutt (1984) (see also Broquet & Wieczorek, 2019). This involves setting the bending moment of a fictive elastic plate equal to that of the bending stresses in a more realistic rheology that considers maximum yielding stresses from fracturing and viscous flow. The bending stresses of the elastic plate can be found analytically if one knows the elastic parameters of the plate and the curvature. For an elastic thickness of 330 km and surface density of 1100 kg m^{-3}, the maximum curvature beneath the north polar cap, defined as the second spatial derivative of the deflection, is 7.4 $\times 10^{-10}$ m^{-1}. The bending stresses of the realistic plate will depend upon its rheology and temperature. For this, we used a wet diabase rheology for the crust, and dry olivine for the mantle (Plesa et al., 2018), a strain rate of 10^{-14} s^{-1} and a low bounding stress of 10 MPa (Phillips et al., 2008), and a thermal conductivity of respectively 3 and 4 W m^{-1} K^{-1} for the crust and mantle.

When computing the temperature profile, we considered the effects of radioactive elements within both the crust and mantle. For the crust, we used the derived surface heat production of 4.9 $\times 10^{-11}$ W kg^{-1} (Hahn et al., 2011) and following Plesa et al. (2018) we set the mantle heat production to 10% of that value. We then simply varied the heat flow at the base of the lithosphere until both bending stresses converged. For an elastic thickness of 330 km, the best-fitting surface heat flow we obtained is 16 mW m^{-2}, which is in good agreement with thermal evolution models from Plesa et al. (2018). Ignoring the presence of radioactive elements in the crust gives a slightly smaller heat flow of 14 mW m^{-2}, where the difference is simply the heat production in the crust (2 mW m^{-2}). Because the crust is thin in the north polar region, the heat flow contribution from the crust is generally low (see also Plesa et al., 2016). If the elastic thickness is set to 450 km, then the heat flow is reduced to 11 mW m^{-2}.

Text S5: Influence and timescale of viscous relaxation

In our deflection model, the lithosphere is purely elastic and the mantle is treated as an inviscid fluid such that shell deformations are instantaneous and not subject to viscous relaxation. The latter is only a valid assumption if the time that has elapsed since the polar cap formed is larger than the time required for viscous adjustments. But, if the age of the polar cap is comparable to the viscous relaxation time, it is possible that the north polar load is in a transient state where the lithosphere is still adjusting viscously. In that case, the present-day topography and flexure reflect not only the current cap geometry but also the time-integrated history of the polar cap load. The loading history of the north polar deposits is potentially complex with cycles of loading and unloading of the lithosphere. In periods of low obliquity, perennial ice forms and in high obliquity periods, ice sublimates and the polar cap decreases in size (Kieffer & Zent, 1992). These periods alternate quickly on million years timescale, as the obliquity of Mars is thought to be mostly chaotic (Jakosky et al., 1995; Laskar et al., 2004).

Crater counting and thickness evolution estimates from Global Climate Models of the north polar deposits agree generally with the idea that the icy deposits are about 1 million years old (Levrard et al., 2007; Herkenhoff & Plaut, 2000). Using the ALMA code of Spada (2008) we computed load Love numbers for a simple four layer Martian interior model based on Phillips et al. (2008). The h' load Love number is a degree (l) dependent linear transfer function that links the load potential (V) to the radial displacement, in our case the deflection (W), as

$$W_{l,m} = \frac{V_{l,m}}{g_0}\, h'_l, \tag{1}$$

where g_0 is the gravitational acceleration at the surface and m is the angular order.

In Figure S6, we show the evolution of the degree-8 load Love number, which corresponds to the scale of the cap, as a function of time. The time before equilibrium is achieved (i.e., the long term asymptote) is found to vary from 10^4 to 10^8 years for mantle viscosities of 10^{19} and 10^{23} Pa s. We note the time to achieve equilibrium depends upon the harmonic degree and would be about 2 times lower for the degree-20 load Love number. The viscosity of the Martian mantle today is thought to range from 10^{20} to 10^{22} Pa s (Plesa et al., 2018), and this limits the time for equilibrium to a range from 10^5 to 10^7 year. This timescale does not allow to rule out the possibility that the polar cap is in a transient state that has not yet achieved equilibrium. As an example, if the north polar cap is 1 million years old and the viscosity of the mantle is 10^{22} Pa s, then it is possible that we are currently observing only about 50% of the final degree-8 deflection below the cap. Assuming that we are observing 50% of the total (i.e. for all degrees) and final deflection below the cap, then the elastic thickness at equilibrium could be as low as 150 km. However, if the cap is 1 million years old and the viscosity of the mantle is 10^{21} Pa s, then our viscoelastic model predicts that the we currently observing the final deflection.

References

Broquet, A., & Wieczorek, M. A. (2019). The gravitational signature of Martian volcanoes. *Journal of Geophysical Research: Planets*, *124*(8), 2054–2086. doi: 10.1029/2019JE005959

Grima, C., Kofman, W., Mouginot, J., Phillips, R. J., Hérique, A., Biccari, D., ... Cutigni, M. (2009). North polar deposits of Mars: Extreme purity of the water ice. *Geophysical Research Letters*, *36*(L03203). doi: https://doi.org/10.1029/

2008GL036326

Hahn, B. C., McLennan, S. M., & Klein, E. C. (2011). Martian surface heat production and crustal heat flow from Mars Odyssey Gamma-Ray spectrometry. *Geophysical Research Letters*, *38*(14). doi: https://doi.org/10.1029/2011GL047435

Herkenhoff, K. E., & Plaut, J. J. (2000). Surface Ages and Resurfacing Rates of the Polar Layered Deposits on Mars. *Icarus*, *144*(2), 243-253. doi: https://doi.org/10.1006/icar.1999.6287

Jakosky, B. M., Henderson, B. G., & Mellon, M. T. (1995). Chaotic obliquity and the nature of the martian climate. *Journal of Geophysical Research: Planets*, *100*(E1), 1579-1584. doi: https://doi.org/10.1029/94JE02801

Kieffer, H. H., & Zent, A. P. (1992). Quasi-periodic climate change on Mars. In H. H. Kieffer, B. M. Jakosky, C. W. Snyder, & M. S. Matthews (Eds.), *Mars* (p. 1180-1218). Univ. of Arizona Press, Tuscon.

Laskar, J., Correia, A., Gastineau, M., Joutel, F., Levrard, B., & Robutel, P. (2004). Long term evolution and chaotic diffusion of the insolation quantities of mars. *Icarus*, *170*(2), 343 - 364. doi: https://doi.org/10.1016/j.icarus.2004.04.005

Levrard, B., Forget, F., Montmessin, F., & Laskar, J. (2007). Recent formation and evolution of northern martian polar layered deposits as inferred from a global climate model. *Journal of Geophysical Research: Planets*, *112*(E6). doi: https://doi.org/10.1016/10.1029/2006JE002772

McNutt, M. K. (1984). Lithospheric flexure and thermal anomalies. *Journal of Geophysical Research: Solid Earth*, *89*(B13), 180–194. doi: https://doi.org/10.1029/

JB089iB13p11180

Nunes, D. C., & Phillips, R. J. (2006). Radar subsurface mapping of the polar layered deposits on mars. *Journal of Geophysical Research: Planets*, *111*(E6). doi: https://doi.org/10.1029/2005JE002609

Pettinelli, E., Vannaroni, G., Cereti, A., Paolucci, F., Della Monica, G., Storini, M., & Bella, F. (2003). Frequency and time domain permittivity measurements on solid co2 and solid co2 soil mixtures as martian soil simulants. *Journal of Geophysical Research: Planets*, *108*(E4). doi: https://doi.org/10.1029/2002JE001869

Phillips, R. J., Zuber, M. T., Smrekar, S. E., Mellon, M. T., Head, J. W., Tanaka, K. L., ... Marinangeli, L. (2008). Mars North Polar Deposits: Stratigraphy, Age, and Geodynamical Response. *Science*, *320*(5880), 1182–1185. doi: https://doi.org/10.1126/science.1157546

Picardi, G., Plaut, J. J., Biccari, D., Bombaci, O., Calabrese, D., Cartacci, M., ... Zampolini, E. (2005). Radar soundings of the subsurface of Mars. *Science*, *310*(5756), 1925–1928. doi: https://doi.org/10.1126/science.1122165

Plesa, A.-C., Grott, M., Tosi, N., Breuer, D., Spohn, T., & Wieczorek, M. A. (2016). How large are present-day heat flux variations across the surface of Mars? *Journal of Geophysical Research: Planets*, *121*(12), 2386–2403. doi: https://doi.org/10.1002/2016JE005126

Plesa, A.-C., Padovan, S., Tosi, N., Breuer, D., Grott, M., Wieczorek, M. A., ... Banerdt, W. B. (2018). The thermal state and interior structure of mars. *Geophysical Research Letters*, *45*(22), 12,198-12,209. doi: https://doi.org/10.1029/2018GL080728

Selvans, M. M., Plaut, J. J., Aharonson, O., & Safaeinili, A. (2010). Internal structure of Planum Boreum, from Mars advanced radar for subsurface and ionospheric sounding data. *Journal of Geophysical Research: Planets*, *115*(E9). doi: https://doi.org/10.1029/2009JE003537

Sihvola, A. (2000, Oct 01). Mixing rules with complex dielectric coefficients. *Subsurface Sensing Technologies and Applications*, *1*(4), 393–415. doi: https://doi.org/10.1023/A:1026511515005

Smith, & Wessel. (1990). Gridding with continuous curvature splines in tension. *Geophysics*, *55*(3), 293-305. doi: https://doi.org/10.1190/1.1442837

Spada, G. (2008). Alma, a fortran program for computing the viscoelastic love numbers of a spherically symmetric planet. *Computers & Geosciences*, *34*(6), 667 - 687. doi: https://doi.org/10.1016/j.cageo.2007.12.001

Wieczorek, M. A. (2008). Constraints on the composition of the Martian south polar cap from gravity and topography. *Icarus*, *196*, 506–517. doi: https://doi.org/10.1016/j.Icarus.2007.10.026

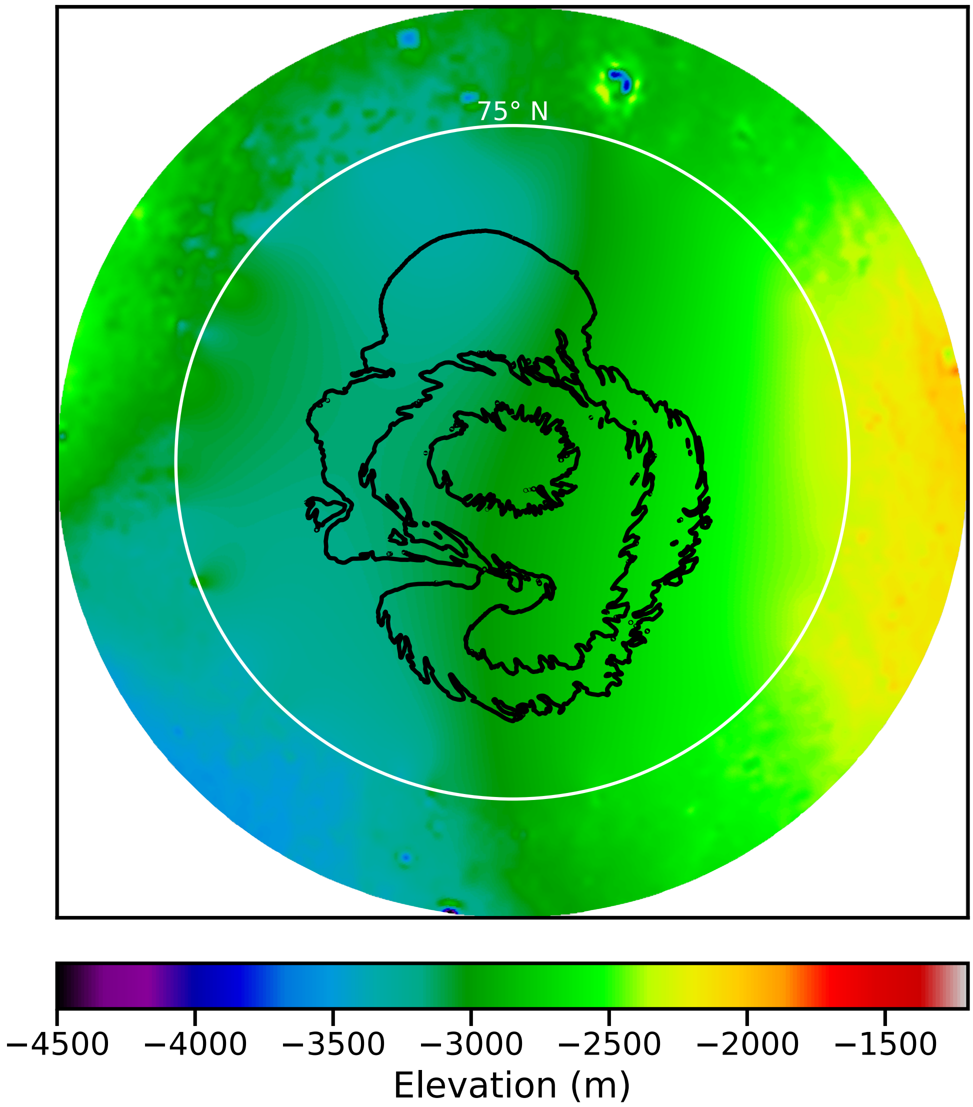

Figure S1. The pre-loading surface poleward 70°N, h_0, estimated using an annulus of MOLA elevation data exterior to the north polar cap between 70°N to 75°N and interpolated poleward using the minimum curvature method of Smith and Wessel (1990). For geologic purposes, elevation contours of the polar cap are shown in black.

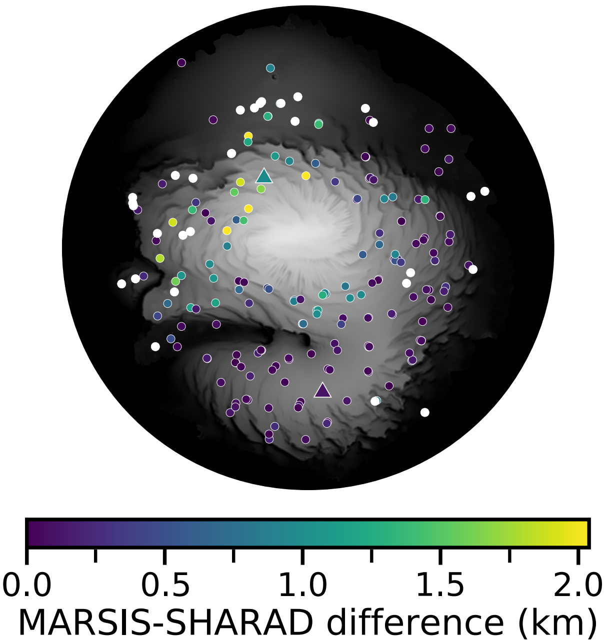

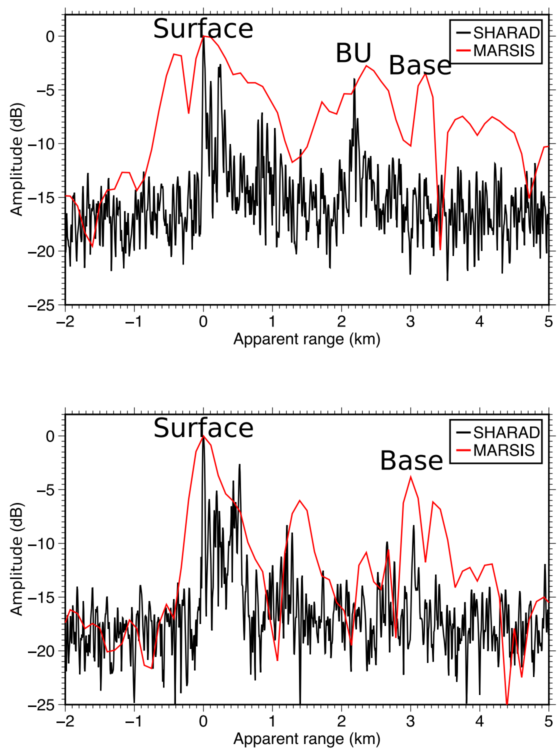

Figure S2. (left) Difference between the apparent thickness of the north polar cap as seen by MARSIS and SHARAD at 213 locals. Circles filled in white show locations where we did not detect a subsurface echo in the SHARAD radargrams. A bimodal distribution is observed, and is due to the inability of SHARAD to see beneath the basal unit when it is present. (right) Echo strength versus the converted apparent range of SHARAD and MARSIS at the location of the 2 triangles (top, latitude 86.26, longitude 212.42, MARSIS orbit 9576, SHARAD orbit 878503 bottom, latitude 81.97, longitude 7.12, MARSIS orbit 3698, SHARAD orbit 3656701) in the left figure. Echoes associated with the reflection from the surface is seen to correlate well between MARSIS and SHARAD. The base of the polar cap is not detected by SHARAD in the upper right image, which is due to the presence of the basal unit.

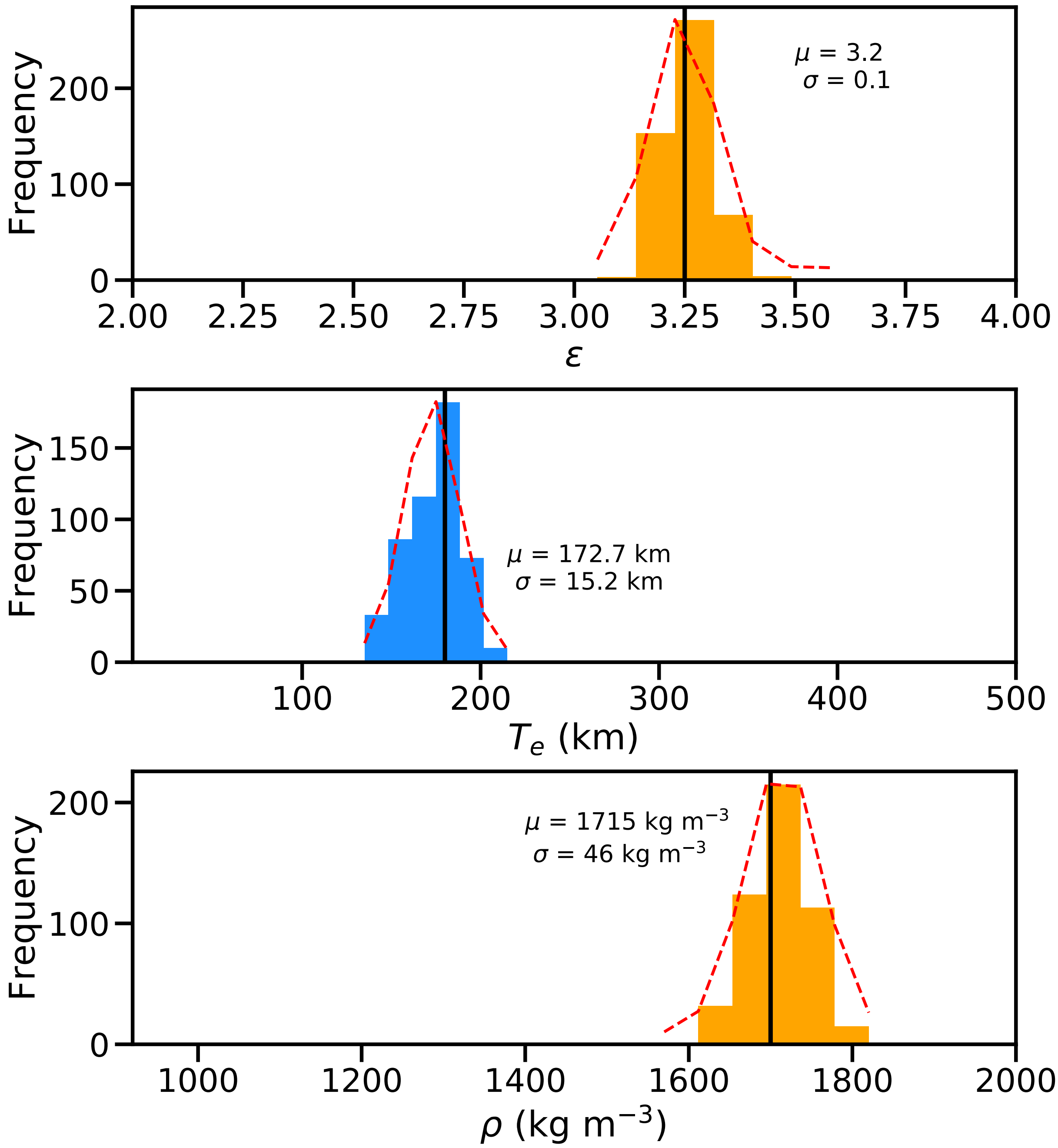

Figure S3. Histograms for the maximum accepted dielectric constant, minimum accepted elastic thickness and maximum accepted ice density following 500 inversions where 50% of the MARSIS data points were randomly selected. The average, μ, and standard deviation, σ, is provided for each of the distributions. The black vertical lines show the inversion results using all MARSIS data points.

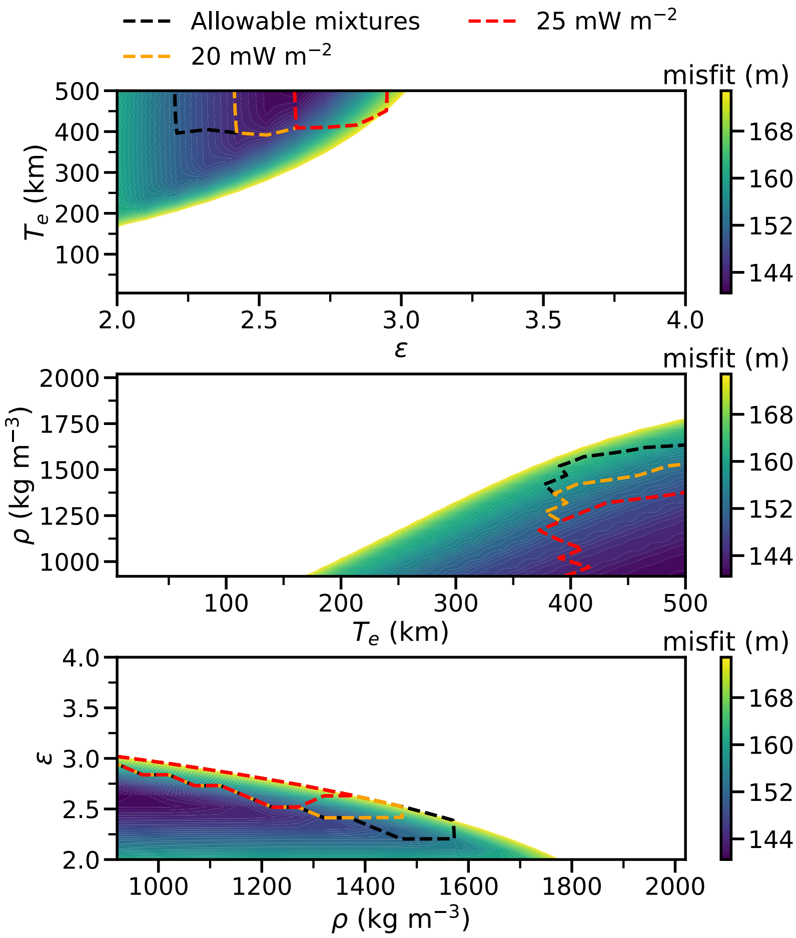

Figure S4. Minimum rms misfit as a function of the dielectric constant (ε), elastic thickness (T_e), and bulk density of the polar cap (ρ) using SHARAD data at 78 locations. The color corresponds to the rms misfit that is cut off at 175 m. The black line delimits possible mixtures, and the red and orange lines delimit those same mixtures that do not produce basal melting for heat flows of 20 and 25 mW m^{-2}. Assuming that the heat flow at the north pole is 20 mW m^{-2}, the real dielectric constant is found to range from 2.4 to 3.0, the elastic thickness is at least 370 km, and the density ranges from 920 to 1570 kg m^{-3}.

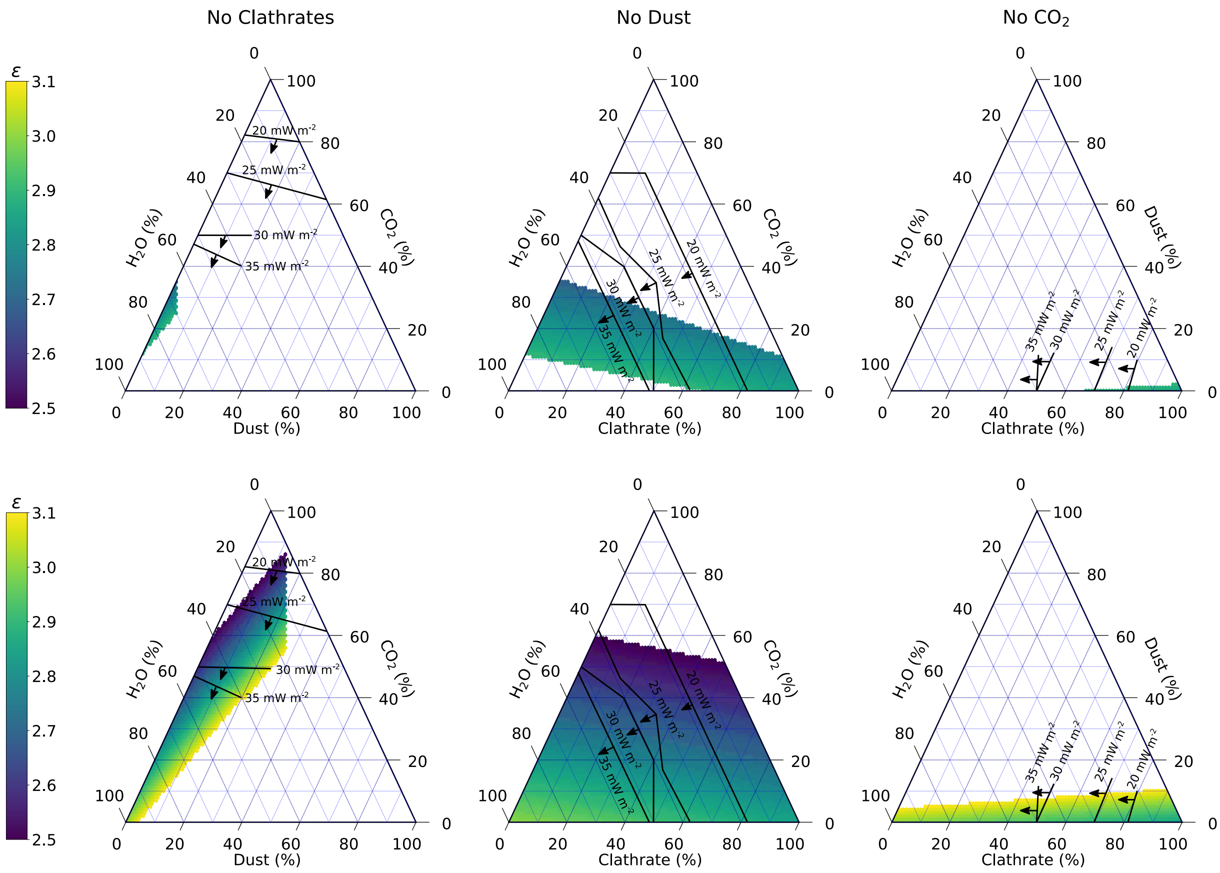

Figure S5. Ternary plots for allowable volumetric mixtures of ices and dust, where one of the four components is absent. Results are shown for two elastic thicknesses, $T_e = 330$ and 400 km (top and bottom), and the color for each allowable mixture corresponds to the real dielectric constant. The black lines limit the regions above witch basal melting would occur as a function of various heat flows from 20 to 35 mW m^{-2}. Acceptable solutions are in the direction given by the black arrows.

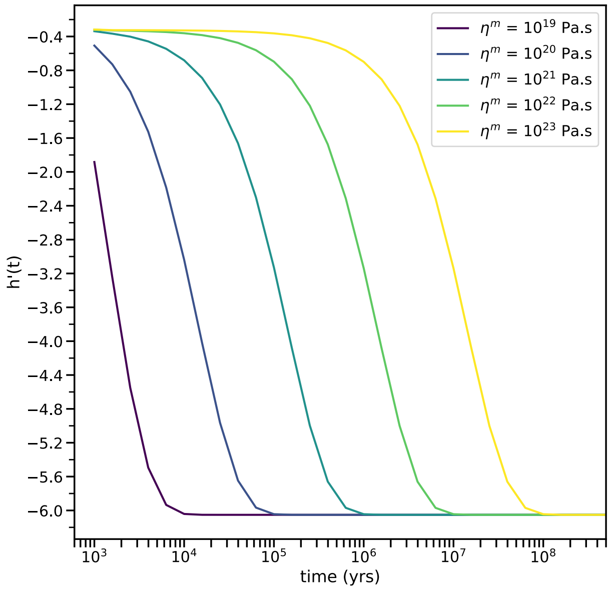

Figure S6. Degree-8 load Love number h' as a function of time for different mantle (η^m) viscosities. The elastic thickness of the lithosphere is set to 330 km, and its rigidity to 40 GPa. Following Phillips et al. (2008), we set the crustal thickness to 35 km, the mantle and core density to respectively 3500 and 6600 kg m^{-3}, and the core radius to 1700 km. A reasonable range for the present-day viscosity of the mantle is 10^{20} to 10^{22} Pa s (Plesa et al., 2018).